Proceedings of The 2021 IEEE International
Conference on Real-time Computing and Robotics
July 15-19, 2021, Xining, China

Inverse Kinematics Formulations of a Continuum Endoscope for a View Adjustment Similar to the da Vinci Endoscope*

Lifei Deng, Zhonghao Wu, *Student Member*, *IEEE*, Yifan Wang, Linhui Wang, and Kai Xu*, *Member, IEEE*

2021 IEEE International Conference on Real-time Computing and Robotics (RCAR) | 978-1-6654-3678-6/21/$31.00 ©2021 IEEE | DOI: 10.1109/RCAR52367.2021.9517626

***Abstract*—Robot-assisted MIS (Minimally Invasive Surgery) attracts significant attention due to its intuitive eye-hand coordination, enhanced dexterity, improved precision, etc. Among the existing multi-port surgical robots, the da Vinci system is considered as a benchmark and enables surgeons to perform delicate operations via several small incisions. The integrated stick-like da Vinci endoscope possesses 4 DoFs (Degrees of Freedom), including two pivoting DoFs around the RCM (Remote Center of Motion) point. On the other hand, continuum manipulators, often with multiple segments, have been applied in surgical applications owing to their design compactness, safe interaction with anatomy, etc. A continuum endoscope usually has two bending segments, and if only one segment is controlled, the change of view is in a different way if compared to the da Vinci endoscope due to the dissimilar motion characteristics. This paper hence investigates the comparison between two inverse kinematics formulations on a proposed two-segment continuum endoscope, regarding the view adjustment such that the field of view of a da Vinci endoscope can be covered as much as possible. The two formulations are based on i) resolved motion rate control, and ii) dimension-reduced inverse kinematics. The numerical experimental results show that when the field of view of a da Vinci endoscope is pivoted around the skin incision within predefined ±60° yaw and pitch ranges, the overlapped visual field with the da Vinci endoscope using the dimension-reduced formulation has an 84.11% improvement compared with the resolved motion rate control.**

I. Introduction

During a da Vinci multi-port surgery procedure, a stick-like da Vinci endoscope is pivoted around the skin incision, a.k.a., the RCM (Remote Center of Motion) point, to realize a 4-DoF (Degree of Freedom) yaw-pitch-roll and translation movement. There are two types of da Vinci endoscopes with 0° or 30° viewing angles. The 30° endoscope is used more widely, as shown in the inset of Fig. 1.

On the other hand, continuum manipulators have been widely investigated in the past decades, demonstrating great potential in the designs of surgical tools due to the inherent compactness and improved dexterity [1-3]. As a crucial component for these vision guided procedures, continuum endoscopes also received a lot of attention in MIS. For example, a common design approach is to use two bending segments to realize an S-shape configuration for visualization [4, 5]. On the other hand, a continuum segment can be added to a stick-like endoscope stem held by an RCM mechanism (e.g., using the da Vinci Research Kit) to realize a 6-DoF endoscope [6, 7].

As abovementioned, continuum endoscopes usually possess multiple segments. While adjusting the view in an MIS procedure, a surgeon usually wants to pan, tilt, rotate or zoom in to a scene. As shown in Fig. 1, the two pivoting DoFs of the da Vinci endoscope are often used to adjust the pan and tilt of the view. If only the distal segment of the continuum endoscope is actuated for the pan and the tilt adjustments, the field of view will be changed dissimilarly even under the same adjustment command from the same initial view, due to the different motion characteristics between the continuum and the da Vinci endoscopes. When a continuum endoscope is used, the surgeons who are familiar with the da Vinci system may experience a prolonged learning curve for adjusting the desired field of view.

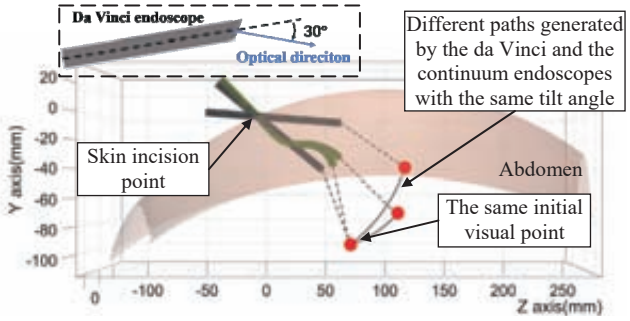

Figure 1. The same tilt angle resulting in different position and orientation changes on the da Vinci and the continuum endoscopes

To realize the same pose changes as the da Vinci endoscope, all the six DoFs of the two-segment continuum endoscope shall be properly controlled. This paper hence investigates different inverse kinematics control approaches on a 6-DoF continuum endoscope to realize a da Vinci-like view adjustment. The first approach is based on the resolved motion rate control [8], while the second one is a dimension-reduced inverse kinematics formulation [9, 10] to deal with configuration variable limits in confined surgical sites.

The rest of this paper is organized as follows. Section II presents the kinematics of the stick-like da Vinci endoscope and the continuum endoscope, while the resolved motion rate

*This work was supported in part by the National Key R&D Program of China (Grant No. 2017YFC0110800), and in part by the National Natural Science Foundation of China (Grant No. 51722507).

Lifei Deng, Yifan Wang and Kai Xu are with School of Mechanical Engineering, Shanghai Jiao Tong University, Shanghai, China, (asterisk indicates the corresponding author, phone:86-21-34206547; emails: qingwa@sjtu.edu.cn, fan_tasy@sjtu.edu.cn and k.xu@sjtu.edu.cn).

Zhonghao Wu is with the RII Lab (Lab of Robotics Innovation and Intervention), UM-SJTU Joint Institute, Shanghai Jiao Tong University, Shanghai, China (emails: zhonghao.wu@sjtu.edu.cn).

Linhui Wang is with the Department of Urology, Shanghai Changhai Hospital, Naval Medical University, Shanghai 200433, China (e-mail: wanglinhuicz@163.com).

control and the dimension-reduced inverse kinematics formulation are elaborated in Section III. Numerical and prototype experiments are reported in Section IV with the conclusions summarized in Section V.

II. Kinematics

The proposed continuum endoscope contains two inextensible continuum segments and has 6-DoF in total as shown in Fig. 2. The two continuum segments are connected by a rigid multi-lumen cylinder and stacked on a base stem, which can be translated along and rotated around its axis, as presented in [11]. The coordinates and nomenclature of both the da Vinci and the continuum endoscopes are presented in Section II.A. The kinematics of the da Vinci endoscope is introduced in Section II.B. The kinematics of a single continuum segment and the 6-DoF continuum endoscope is elaborated in Section II.C and Section II.D, respectively.

A. Coordinates and Nomenclature

The nomenclature of the da Vinci and the continuum endoscope is listed in Table I. The coordinates of the da Vinci model, the t^{th} continuum segment, and the entire continuum endoscope are shown in Fig. 2(a), Fig. 2(b), and Fig. 2(c), respectively.

- *World Coordinate* $\{w\}=\{\hat{\mathbf{x}}_w,\hat{\mathbf{y}}_w,\hat{\mathbf{z}}_w\}$ is located at the skin incision point.
- *The da Vinci Endoscope's Coordinate* 1, 2, 3 $\{dV1\}=\{\hat{\mathbf{x}}_{dV1},\hat{\mathbf{y}}_{dV1},\hat{\mathbf{z}}_{dV1}\}$, $\{dV2\}=\{\hat{\mathbf{x}}_{dV2},\hat{\mathbf{y}}_{dV2},\hat{\mathbf{z}}_{dV2}\}$, $\{dV3\}=\{\hat{\mathbf{x}}_{dV3},\hat{\mathbf{y}}_{dV3},\hat{\mathbf{z}}_{dV3}\}$ share the same origin with $\{w\}$, under a yaw-pitch-roll rotation around their axes with respect to the current frames.
- *The da Vinci Endoscope's End Coordinate* $\{dVe\}=\{\hat{\mathbf{x}}_{dVe},\hat{\mathbf{y}}_{dVe},\hat{\mathbf{z}}_{dVe}\}$ attaches its origin at the end of the stick-like stem under a pure translation from $\{dV3\}$.
- *Base Coordinate of the* t^{th} *segment* $\{tb\}=\{\hat{\mathbf{x}}_{tb},\hat{\mathbf{y}}_{tb},\hat{\mathbf{z}}_{tb}\}$ locates its origin at the center of the base ring of the t^{th} segment. $\hat{\mathbf{z}}_{tb}$ is perpendicular to the base ring with $\hat{\mathbf{x}}_{tb}$ passing through the first backbone. $\{1b\}$ is translated along and axially rotated around the $\hat{\mathbf{z}}_w$ with a length of L_0 and an angle of φ from $\{w\}$.
- *Bending Plane Coordinate* 1 *of the* t^{th} *segment* $\{t1\}=\{\hat{\mathbf{x}}_{t1},\hat{\mathbf{y}}_{t1},\hat{\mathbf{z}}_{t1}\}$ is attached at the base ring of the t^{th} segment. $\hat{\mathbf{x}}_{t1}$ is aligned with $\hat{\mathbf{z}}_{tb}$ so that the XY plane is aligned with the bending plane.
- *Bending Plane Coordinate* 2 *of the* t^{th} *segment* $\{t2\}=\{\hat{\mathbf{x}}_{t2},\hat{\mathbf{y}}_{t2},\hat{\mathbf{z}}_{t2}\}$ is achieved from $\{t1\}$ via a rotation around $\hat{\mathbf{z}}_{t1}$ of an angle θ_t, with its origin set at the center of the end ring of the t^{th} segment.
- *End Coordinate of the* t^{th} *segment* $\{te\}=\{\hat{\mathbf{x}}_{te},\hat{\mathbf{y}}_{te},\hat{\mathbf{z}}_{te}\}$ shares the same origin with $\{t2\}$. Its XY plane coincides with the end ring where $\hat{\mathbf{x}}_{te}$ points to the first backbone.

TABLE I. Nomenclature Used in this Paper

Symbol	Definition
L_{dV}	Length of the da Vinci endoscope extended into the abdomen.
μ_{yaw}	Yaw angle, right-handed rotation angle about $\hat{\mathbf{y}}_w$.
μ_{pitch}	Pitch angle, right-handed rotation angle about $\hat{\mathbf{x}}_{dV1}$.
μ_{roll}	Roll angle, right-handed rotation angle about $\hat{\mathbf{z}}_{dV2}$.
α	Right-hand angle between the optical axis of the camera to the axis of the endoscope.
β	Angle between the da Vinci endoscope stem and the line connecting with the RCM point and the camera.
t	Index of segment, t = 1 or 2.
φ	Right-handed rotation angle of the base stem.
θ_t	Bending angle of the t^{th} segment in the bending plane.
δ_t	The right-handed rotation angle from the bending plane to $\hat{\mathbf{x}}_{tb}$ about $\hat{\mathbf{z}}_{tb}$.
L_t	Length of the virtual central backbone of the t^{th} segment.
L_0, L_m, L_c	Length of the base stem, the multi-lumen cylinder between the two continuum segments, and the camera length.
$\mathbf{\Psi}_0$	$\mathbf{\Psi}_0=[L_0\ \varphi]^T$ is the configuration vector for the base stem.
$\mathbf{\Psi}_t$	$\mathbf{\Psi}_t=[\theta_t\ \delta_t]^T$ is the configuration vector for t^{th} segment.
$\mathbf{\Psi}$	$\mathbf{\Psi}=[\mathbf{\Psi}_0{}^T\mathbf{\Psi}_1{}^T\mathbf{\Psi}_2{}^T]^T$ is the configuration vector for the entire 6-DoF endoscope.
$\mathbf{J}_t$	Jacobian matrix mapping from configuration space to task space for segment t. $\mathbf{J}_t=[\mathbf{J}_{tv}{}^T\ \mathbf{J}_{t\omega}{}^T]^T$, where $\mathbf{J}_{tv}$ and $\mathbf{J}_{t\omega}$ are the linear and angular velocity items, respectively.
L_e	Effective maximum view distance along the optical axis.

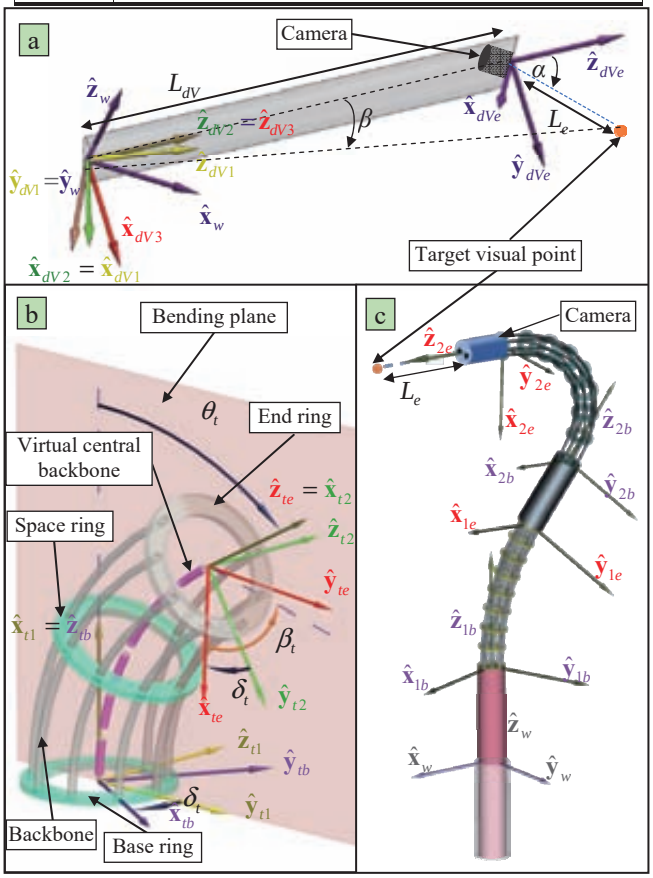

Figure 2. Nomenclature and coordinates of (a) the da Vinci endoscope, (b) the t^{th} continuum segment [11], and (c) the 6-DoF continuum endoscope

The variable ranges and structural parameters for the da Vinci and the continuum endoscopes are listed in Table II.

TABLE II. STRUCTURAL PARAMETERS AND VARIABLE RANGES

Types	Symbol	Values and ranges
Da Vinci endoscope	μ_{yaw}	[-π/3, π/3]
	μ_{pitch}	[-π/3, π/3]
	μ_{roll}	[-π, π]
	α	π/6
	L_{dV}	[0,100] mm
Continuum endoscope	φ	[-π, π]
	θ_1	[0, π/4]
	θ_2	[0, π/2]
	L_0	[0,100] mm
	L_1	20 mm
	L_m	6 mm
	L_2	30 mm
	L_c	20 mm
Both endoscopes	L_e	120 mm

B. Forward Kinematics of the da Vinci Endoscope

A da Vinci endoscope has four DoFs: yaw-pitch-roll rotation DoFs and a translational DoF, as shown in Fig. 2(a). The camera is mounted on the stem tip, with a fixed deviation angle of α about $\hat{\mathbf{x}}_{dVe}$. The orientation of the da Vinci endoscope while watching the target visual point is hence defined as a rotation about $\hat{\mathbf{x}}_{dVe}$ from $\{dVe\}$ as in (1), with the position set along the optical axis of the camera with a distance L_e as in (2).

$$ {}^{w}\mathbf{R}_{dVt} = {}^{w}\mathbf{R}_{dV1}\,{}^{dV1}\mathbf{R}_{dV2}\,{}^{dV2}\mathbf{R}_{dV3}\,{}^{dV3}\mathbf{R}_{dVe}\mathbf{R}_{\hat{\mathbf{x}}}(\alpha) \tag{1} $$

$$ {}^{w}\mathbf{p}_{dVt} = {}^{w}\mathbf{R}_{dV1}\,{}^{dV1}\mathbf{R}_{dV2}\,{}^{dV2}\mathbf{R}_{dV3}\left({}^{dV3}\mathbf{p}_{dVe} + {}^{dV3}\mathbf{R}_{dVe}\,{}^{dVe}\mathbf{p}_{dVt}\right) \tag{2} $$

Where ${}^{w}\mathbf{R}_{dV1} = \mathbf{R}_{\hat{\mathbf{y}}}(\mu_{\text{yaw}})$, ${}^{dV1}\mathbf{R}_{dV2} = \mathbf{R}_{\hat{\mathbf{x}}}(\mu_{\text{pitch}})$, ${}^{dV2}\mathbf{R}_{dV3} = \mathbf{R}_{\hat{\mathbf{z}}}(\mu_{\text{roll}})$, ${}^{dV3}\mathbf{R}_{dVe} = \mathbf{I}_{3\times3}$; $\mathbf{R}_{\hat{\mathbf{x}}}(\cdot)$ represents a simple rotation about $\hat{\mathbf{x}}$. ${}^{dV3}\mathbf{p}_{dVe} = [0\ 0\ L_{dV}]^T$ and ${}^{dVe}\mathbf{p}_{dVt} = L_e[0\ \sin(\alpha)\ \cos(\alpha)]^T$.

C. Forward Kinematics of a Single Continuum Segment

According to the constant curvature bending assumption, the shape of a single continuum segment can be characterized as a circular arc [12, 13]. The forward kinematics of a single segment is summarized as follows.

The position of $\{te\}$ with respect to $\{tb\}$ is as follows.

$$ {}^{tb}\mathbf{p}_{te} = \frac{L_t}{\theta_t}\begin{bmatrix}\cos\delta_t(1-\cos\theta_t) & \sin\delta_t(\cos\theta_t-1) & \sin\theta_t\end{bmatrix}^T \tag{3} $$

Where ${}^{tb}\mathbf{p}_{te} = [0\ 0\ L_t]^T$, when θ_t equals 0. The rotation matrix from $\{tb\}$ to $\{te\}$ is presented in (4).

$$ {}^{tb}\mathbf{R}_{te} = {}^{tb}\mathbf{R}_{t1}\,{}^{t1}\mathbf{R}_{t2}\,{}^{t2}\mathbf{R}_{te} \tag{4} $$

Where ${}^{tb}\mathbf{R}_{t1} = \mathbf{R}_{\hat{\mathbf{z}}}(-\delta)\mathbf{R}_{\hat{\mathbf{x}}}(-\pi/2)\mathbf{R}_{\hat{\mathbf{z}}}(-\pi/2)$, ${}^{t1}\mathbf{R}_{t2} = \mathbf{R}_{\hat{z}}(\theta)$, ${}^{t2}\mathbf{R}_{te} = {}^{tb}\mathbf{R}_{t1}^{T}$.

The Jacobian matrix is presented as follows.

$$ \mathbf{J}_{t\mathbf{v}} = L_t\begin{bmatrix}\cos\delta_t\left(\dfrac{\cos\theta_t-1}{\theta_t^2}+\dfrac{\sin\theta_t}{\theta_t}\right) & \dfrac{\sin\delta_t}{\theta_t}(\cos\theta_t-1)\\ \sin\delta_t\left(\dfrac{1-\cos\theta_t}{\theta_t^2}-\dfrac{\sin\theta_t}{\theta_t}\right) & \dfrac{\cos\delta_t}{\theta_t}(\cos\theta_t-1)\\ -\dfrac{\sin\theta_t}{\theta_t^2}+\dfrac{\cos\theta_t}{\theta_t} & 0\end{bmatrix} \tag{5} $$

$$ \mathbf{J}_{t\boldsymbol{\omega}} = \begin{bmatrix}\sin\delta_t & \cos\delta_t\sin\theta_t\\ \cos\delta_t & -\sin\delta_t\sin\theta_t\\ 0 & \cos\theta_t-1\end{bmatrix} \tag{6} $$

$\mathbf{J}_{t\mathbf{v}}$ and $\mathbf{J}_{t\boldsymbol{\omega}}$ are the linear and angular velocity components of the Jacobian matrix. When θ_t is close to 0, $\mathbf{J}_{t\mathbf{v}}$ and $\mathbf{J}_{t\boldsymbol{\omega}}$ can be derived under the L'Hôpital's rule.

D. Forward Kinematics of the 6-DoF Continuum Endoscope

As shown in Fig. 2(c), the kinematics of the continuum endoscope is defined in $\{w\}$. The orientation of the continuum endoscope while watching the target visual point is $\{2e\}$ as shown in (7), while the position is defined along the optical axis of the camera with a distance L_e as in (8).

$$ {}^{w}\mathbf{R}_{ct} = {}^{w}\mathbf{R}_{1b}\,{}^{1b}\mathbf{R}_{1e}\,{}^{1e}\mathbf{R}_{2b}\,{}^{2b}\mathbf{R}_{2e} \tag{7} $$

$$ {}^{w}\mathbf{p}_{ct} = {}^{w}\mathbf{p}_{1b} + {}^{w}\mathbf{R}_{1b}\left({}^{1b}\mathbf{p}_{1e} + {}^{1b}\mathbf{R}_{1e}\left({}^{1e}\mathbf{p}_{2b} + {}^{1e}\mathbf{R}_{2b}\left({}^{2b}\mathbf{p}_{2e} + {}^{2b}\mathbf{R}_{2e}\,{}^{2e}\mathbf{p}_{ct}\right)\right)\right) \tag{8} $$

Where ${}^{1b}\mathbf{R}_{1e}$ and ${}^{2b}\mathbf{R}_{2e}$ are defined in (4), ${}^{1b}\mathbf{p}_{1e}$ and ${}^{2b}\mathbf{p}_{2e}$ are defined in (3). The rest items in (7) and (8) are listed as below.

- According to the definition of $\{tb\}$, ${}^{w}\mathbf{R}_{1b} = \mathbf{R}_{\hat{z}}(\varphi)$, ${}^{w}\mathbf{p}_{1b} = [0\ 0\ L_0]^T$.
- $\{1e\}$ and $\{2b\}$ are connected by a multi-lumen cylinder, therefore, ${}^{1e}\mathbf{R}_{2b} = \mathbf{I}_{3\times3}$, ${}^{1e}\mathbf{p}_{2b} = [0\ 0\ L_m]^T$.
- The visual point is along $\hat{\mathbf{z}}_{2e}$ in $\{2e\}$ by a length of $L_c + L_e$: ${}^{2e}\mathbf{p}_{ct} = [0\ 0\ L_c + L_e]^T$.

The Jacobian matrix of the two-segment continuum endoscope is then derived with respect to $\{w\}$.

$$ \mathbf{J} = \begin{bmatrix}\mathbf{T}_0 & {}^{w}\mathbf{R}_{1b}\mathbf{T}_1 & {}^{w}\mathbf{R}_{1b}\,{}^{1b}\mathbf{R}_{1e}\,{}^{1e}\mathbf{R}_{2b}\mathbf{T}_2\\ \mathbf{J}_{0\boldsymbol{\omega}} & {}^{w}\mathbf{R}_{1b}\mathbf{J}_{1\boldsymbol{\omega}} & {}^{w}\mathbf{R}_{1b}\,{}^{1b}\mathbf{R}_{1e}\,{}^{1e}\mathbf{R}_{2b}\mathbf{J}_{2\boldsymbol{\omega}}\end{bmatrix} \tag{9} $$

Where $\mathbf{T}_0 = \mathbf{J}_{0\mathbf{v}} - ({}^{w}\mathbf{R}_{1b}\,{}^{1b}\mathbf{p}_{ct})^{\wedge}\mathbf{J}_{0\boldsymbol{\omega}}$, $\mathbf{T}_1 = \mathbf{J}_{1\mathbf{v}} - ({}^{1b}\mathbf{R}_{1e}\,{}^{1e}\mathbf{p}_{ct})^{\wedge}\mathbf{J}_{1\boldsymbol{\omega}}$, and $\mathbf{T}_2 = \mathbf{J}_{2\mathbf{v}} - ({}^{2b}\mathbf{R}_{2e}\,{}^{2e}\mathbf{p}_{ct})^{\wedge}\mathbf{J}_{2\boldsymbol{\omega}}$. The operator $(\mathbf{p})^{\wedge}$ returns the skew-symmetric matrix of the vector $\mathbf{p}$.

III. INVERSE KINEMATICS CONTROL

In order to realize a da Vinci-like view adjustment, two approaches are investigated. The first one is the conventional resolved motion rate control [8], while the second is the dimension-reduced inverse kinematics formulation [9, 10], as presented in Section III.A and Section III.B, respectively.

A. Resolved Motion Rate Control

Referring to [8], the flowchart of the resolved motion rate is presented in Fig. 3(a). The target position ${}^{w}\mathbf{p}_{dVt}$ and the

target orientation ${}^{w}\mathbf{R}_{dVt}$ are set from the forward kinematics of the da Vinci endoscope. The position error $\varepsilon_{\mathbf{p}}$ and orientation error $\varepsilon_{\mathbf{R}}$ are the discrepancy between the target pose and the position ${}^{w}\mathbf{p}_{ct}$ and orientation ${}^{w}\mathbf{R}_{ct}$ of the continuum endoscope.

$$\begin{cases} \varepsilon_{\mathbf{p}} = \left\| {}^{w}\mathbf{p}_{dVt} - {}^{w}\mathbf{p}_{ct} \right\| \\ \varepsilon_{\mathbf{R}} = \mathrm{rot}_{\theta}^{-1}({}^{w}\mathbf{R}_{dVt}\,{}^{w}\mathbf{R}_{ct}^{T}) \end{cases} \tag{10}$$

Where $\mathrm{rot}_{\theta}^{-1}(\mathbf{R})$ gives the angle component of axis-angle representation of a rotation matrix $\mathbf{R}$.

The desired velocities ${}^{w}\mathbf{v}_{ct}$ and ${}^{w}\boldsymbol{\omega}_{ct}$ of the continuum endoscope are defined as in (11).

$$\begin{cases} {}^{w}\mathbf{v}_{ct} = v_{\lim}({}^{w}\mathbf{p}_{dVt} - {}^{w}\mathbf{p}_{ct})/\varepsilon_{\mathbf{p}} \\ {}^{w}\boldsymbol{\omega}_{ct} = \omega_{\lim}\mathrm{rot}_{\hat{\mathbf{r}}}^{-1}({}^{w}\mathbf{R}_{dVt}\,{}^{w}\mathbf{R}_{ct}^{T}) \end{cases} \tag{11}$$

Where $v_{\lim}$ and $\omega_{\lim}$ are the preset constant scalars linear and angular velocities and $\mathrm{rot}_{\hat{\mathbf{r}}}^{-1}(\mathbf{R})$ gives the axis component of axis-angle representation of $\mathbf{R}$.

The rates of the configuration vector of the continuum endoscope is calculated from a twist vector ${}^{w}\dot{\mathbf{x}}_{ct}$ as shown in (12).

$$\dot{\boldsymbol{\psi}} = \mathbf{J}^{\dagger\,w}\dot{\mathbf{x}}_{ct} = \mathbf{J}^{\dagger}\begin{bmatrix} {}^{w}\mathbf{v}_{ct}^{T} & {}^{w}\boldsymbol{\omega}_{ct}^{T} \end{bmatrix}^{T} \tag{12}$$

Where $\mathbf{J}^{\dagger}$ is the Moore–Penrose pseudoinverse inverse matrix.

The configuration vector of the continuum endoscope will then be updated with an increment as in (13).

$$\boldsymbol{\psi} = \boldsymbol{\psi} + \dot{\boldsymbol{\psi}}\Delta t \tag{13}$$

However, if the updated configuration variables violate their limits, a compulsory reassignment will be implemented to hold the variables at their limits. A position and/or orientation deviation may hence appear.

B. Dimension-Reduced Inverse Kinematics Control

Since the continuum endoscope's motion may not fully cover those of the da Vinci endoscope, the configuration variables of the continuum endoscope may often approach their limits. When a limit is reached, if the corresponding configuration variable is simply bounded at the limit value as in the resolved motion rate control, the visual trajectory may deviate from the desired pose. The dimension-reduced inverse kinematics formulation handles such a situation via a partial mapping from the configuration space to the task space only involving the non-saturated variables. Such a formulation also often uses prioritization, as derived below.

The Jacobian for the 6-DoF continuum manipulator can be expressed by its column vector.

$$\mathbf{J} = \begin{bmatrix} \mathbf{j}_1 & \mathbf{j}_2 & \mathbf{j}_3 & \mathbf{j}_4 & \mathbf{j}_5 & \mathbf{j}_6 \end{bmatrix} \tag{14}$$

When the ξ^{th} configuration variable approaches the limit, this proposed algorithm will fix the value of the ξ^{th} configuration variable at the last iteration value, and remove the corresponding column $\mathbf{j}_{\xi}$ from $\mathbf{J}$. The corresponding item in $\boldsymbol{\psi}$ and $\dot{\boldsymbol{\psi}}$ is also removed. The modified Jacobian matrix and the modified configuration vector are as follows.

$$\tilde{\mathbf{J}} = \begin{bmatrix} \mathbf{j}_1 & \cdots & \mathbf{j}_{\xi-1} & \mathbf{j}_{\xi+1} & \cdots & \mathbf{j}_6 \end{bmatrix} \tag{15}$$

$$\dot{\tilde{\boldsymbol{\psi}}} = \begin{bmatrix} \dot{\psi}_1 & \cdots & \dot{\psi}_{\xi-1} & \dot{\psi}_{\xi+1} & \cdots & \dot{\psi}_6 \end{bmatrix}^{T} \tag{16}$$

Since the number of the active components of $\dot{\tilde{\boldsymbol{\psi}}}$ is less than the number of target space twist $\dot{\mathbf{x}}$, the linear and angular velocity cannot be satisfied simultaneously. To get closer to the target position, the linear velocity is set with a higher priority compared with the angular one. This algorithm uses a prioritized-Jacobian to achieve the desired configuration space velocity [14].

$$\begin{aligned} \dot{\tilde{\boldsymbol{\psi}}} &= \begin{bmatrix} \dot{\psi}_1 & \cdots & \dot{\psi}_{\xi-1} & \dot{\psi}_{\xi+1} & \cdots & \dot{\psi}_6 \end{bmatrix}^{T} \\ &= \tilde{\mathbf{J}}_{\mathbf{v}}^{\dagger\,w}\mathbf{v}_t + \left[\tilde{\mathbf{J}}_{\boldsymbol{\omega}}(\mathbf{I} - \tilde{\mathbf{J}}_{\mathbf{v}}^{\dagger}\tilde{\mathbf{J}}_{\mathbf{v}})\right]^{\dagger}({}^{w}\boldsymbol{\omega}_t - \tilde{\mathbf{J}}_{\boldsymbol{\omega}}\tilde{\mathbf{J}}_{\mathbf{v}}^{\dagger\,w}\mathbf{v}_t) \end{aligned} \tag{17}$$

Where $\tilde{\mathbf{J}}_{\mathbf{v}}$ and $\tilde{\mathbf{J}}_{\boldsymbol{\omega}}$ are the linear and angular components of modified Jacobian $\tilde{\mathbf{J}}$.

The modified configuration vector is similarly updated as in (13).

$$\tilde{\boldsymbol{\psi}} = \tilde{\boldsymbol{\psi}} + \dot{\tilde{\boldsymbol{\psi}}}\Delta t \tag{18}$$

Furthermore, when an updated configuration variable in $\tilde{\boldsymbol{\psi}}$ violates the limit, the corresponding column of the modified Jacobian matrix needs to be further removed until all variables are within their ranges, as illustrated in Fig. 3(b).

When the Jacobian matrix becomes singular, a singularity robust formulation is implemented.

$$\mathbf{J}^{+} = \mathbf{J}^{T}(\mathbf{J}\mathbf{J}^{T} + \lambda\mathbf{I})^{-1} \tag{19}$$

Where λ is a constant damping coefficient. In this study, λ is set as 0.01.

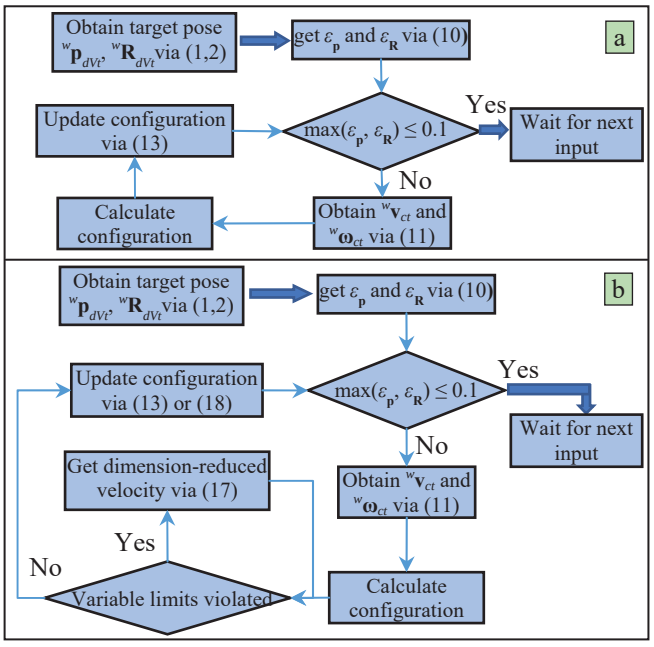

Figure 3. Flowcharts of (a) the resolved motion rate control, and (b) the dimension-reduced inverse kinematics formulation

IV. Experiments

The effective view distance of the endoscope camera ranges from 30 mm to 120 mm and the FOV (field of view) is 90°. Therefore, a pyramidal frustum shape is formed to model

the visual field. To evaluate the capability of the continuum endoscope tracking the da Vinci one, an OR (overlapping ratio) index is defined as the overlapped volume of the two pyramidal frustums with respect to the volume of a single pyramidal frustum. The calculation of the overlapped volume uses the convexHull function from MATLAB.

In all the simulations, the velocity limits of the continuum endoscope are set at 100 mm/s for the linear velocity limit and $\pi/2$ rad/s for the angular velocity limit.

A. *Two Simulation Case Studies*

The continuum endoscope in both case studies starts from the same initial configuration: L_0 = 8 mm, φ = 0 rad, θ_1 = 0.3857 rad, δ_1 = -1.57 rad, θ_2 = 0.7828 rad, δ_2 = 1.57 rad.

In the first case study, the joint values of the tracked da Vinci endoscope are L_{dV} = 60.88 mm, μ_{yaw} = 0.5 rad, μ_{pitch} = -0.4 rad, and μ_{roll} = 0 rad. The process for the continuum endoscope to reach the FOV of the da Vinci endoscope is shown in Fig. 4(a) with the configuration variable trajectories shown in Fig. 5(a). It can be seen that the configuration variables θ_1, θ_2, and L_0 in the resolved motion rate control are sequentially stuck at their limits, and the position and orientation errors fail to converge. However, the dimension-reduced inverse kinematics formulation converged even when θ_1 and θ_2 reached their limits. Therefore, the obtained field of view in the resolved motion rate control has a smaller overlapped visual volume with the da Vinci endoscope, compared with the dimension-reduced inverse kinematics formulation, as shown in Fig. 4(a). The da Vinci endoscope is represented by the black stem, with its visual field indicated by the red pyramidal frustum. The green segment and pyramidal frustum are drawn to represent the continuum endoscope and its field of view.

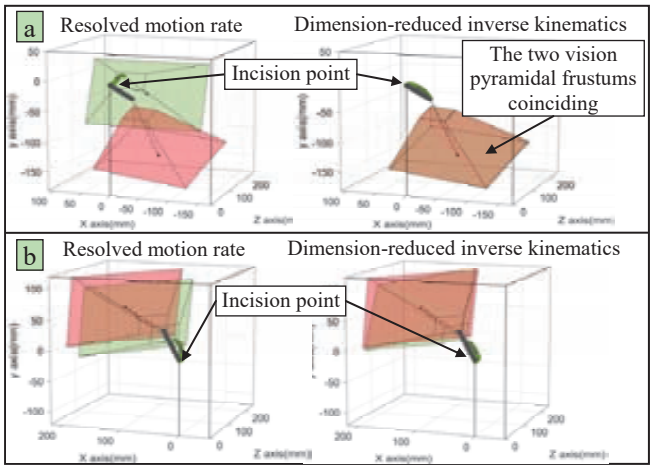

Figure 4. Comparison results when the target pose is (a) inside and (b) outside the continuum endoscope's workspace

In the second case, the target pose is out of the continuum endoscope's workspace, and the joint values of the da Vinci endoscope are L_{dV} = 62.5mm, μ_{yaw} = -0.9 rad, μ_{pitch} = 0.7 rad, and μ_{roll} = 0 rad. When θ_1 reaches the limit, since the position is assigned with a higher priority, the position error in the dimension-reduced inverse kinematics formulation converges to zero with a minimized orientation error. Hence, the OR in the dimension-reduced formulation is still higher than that in the resolved motion rate control. The converged results and the trajectories of the configuration variables are shown in Fig. 4(b) and Fig. 5(b), respectively.

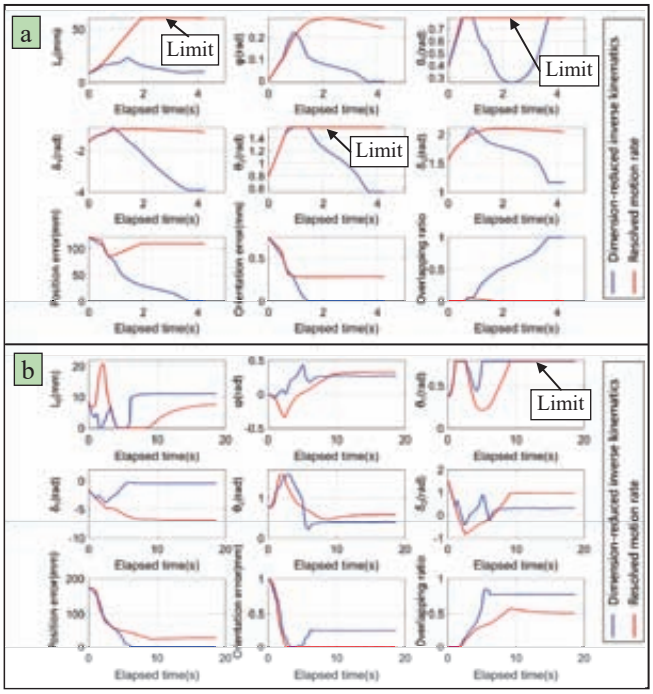

Figure 5. Plots of the configuration variables, the position and the orientation errors, the OR using the two methods in (a) the first and (b) the second case studies

B. *Coverage of the Field of View*

To indicate the overall coverage of the FOV of the da Vinci Endoscope, two coverage maps were generated using the resolved motion rate control and the dimension-reduced inverse kinematics formulation, as shown in Fig. 6. The target visual poses are defined where the stem of the da Vinci endoscope is continuously pivoted around the RCM, traversing the yaw and pitch motion ranges from Table II with L_{dV} set at 65 mm. Each point in Fig. 6 is a target visual point and its color indicates the OR index that is generated using the two methods, referring to the color bar in Fig. 6.

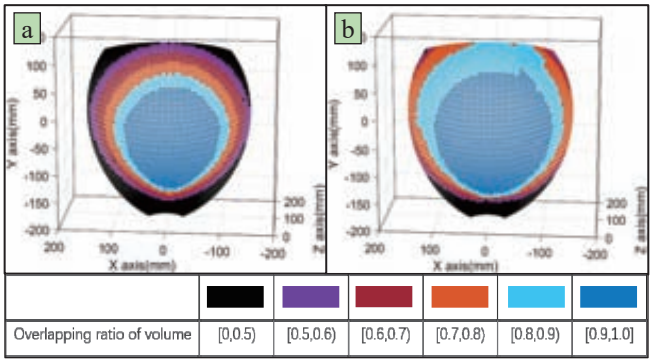

Figure 6. The overlapping map under (a) the resolved motion rate control and (b) the dimension-reduced inverse kinematics formulation

It can be seen that good tracking results occur around the center of the task space, and the OR declines as the target visual point moves away from the center in both methods

where the configuration variables move towards their corresponding limits.

In this study, the OR index is considered to be acceptable when it is larger than 0.8. The acceptable area obtained from the dimension-reduced formulation is 61.07%, with an 84.11% improvement compared with the 33.17% acceptable area in the resolved motion rate control.

C. Prototype Experiments

A two-segment continuum endoscope was mounted on an actuation unit as shown in Fig. 7 and a Micron Tracker SX60 (Claron Tech Inc.) is used to detect the actual poses of Marker #I & #II. Marker #I was mounted on the camera for calculating the target visual point. Marker #II was attached to the trocar. The position of the camera and the target visual point is hence obtained in $\{w\}$.

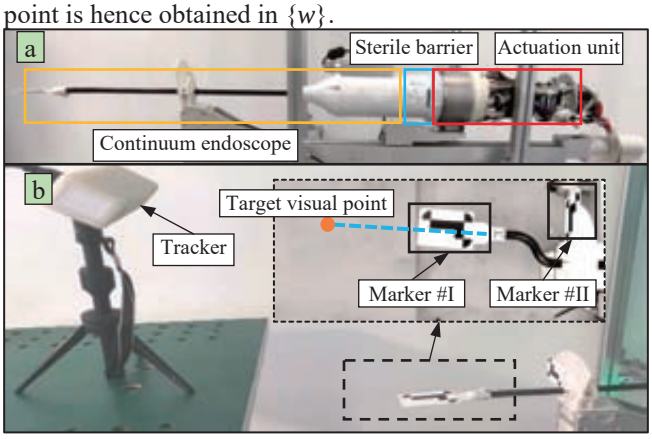

Figure 7. Experimental setup: (a) the proposed 6-DoF continuum endoscope, (b) the tracking system

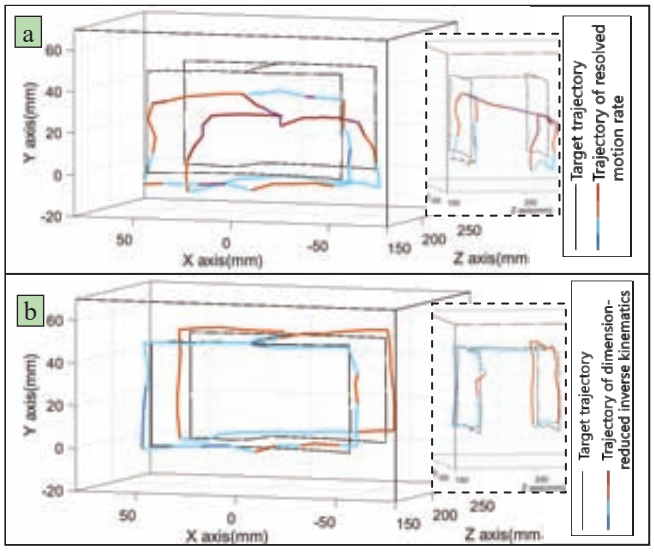

Figure 8. Actual trajectories of the target visual points of the continuum endoscope under (a) the resolved motion rate control, and (b) the dimension-reduced inverse kinematics formulation

The target visual points are defined along a cuboid of 100 mm × 50 mm × 50 mm, generated by the forward kinematics of the da Vinci endoscope. The actual trajectories of the target visual points of the continuum endoscope using the two methods are plotted in Fig. 8, where the color indicates the OR index from the color bar in Fig. 6. It is clear that the dimension-reduced formulation generates the actual vision trajectories closer to the target ones. And the errors in Fig. 8(b) are primarily from the positioning accuracy of the prototype.

V. Conclusions

In this paper, two inverse kinematics formulations are investigated on a 6-DoF continuum endoscope to achieve a view adjustment similar to the da Vinci endoscope. As the conventional resolved motion rate control may fail to converge when the configuration variables are around their limits, the dimension-reduced inverse kinematics formulation is introduced for improved performances. The experimental results showed that the dimension-reduced formulation has an improvement of 84.11% compared with the resolved motion rate control. It is expected that the dimension-reduced formulation is to be implemented into the actual surgical system to realize a view adjustment similar to that of the da Vinci endoscope in the near future.

References

[1] P. E. Dupont, J. Lock, B. Itkowitz, and E. Butler, "Design and Control of Concentric-Tube Robots," *IEEE Transactions on Robotics,* Vol. 26, No.2, pp. 209-225, April 2010.

[2] K. Xu, J. Zhao, and M. Fu, "Development of the SJTU Unfoldable Robotic System (SURS) for Single Port Laparoscopy," *IEEE/ASME Transactions on Mechatronics,* Vol. 20, No.5, pp. 2133-2145, 2015.

[3] T.-D. Nguyen and J. Burgner-Kahrs, "A Tendon-Driven Continuum Robot with Extensible Sections," in *IEEE/RSJ International Conference on Intelligent Robots and Systems (IROS)*, Hamburg, Germany, 2015, pp. 2130-2135.

[4] S. Can, C. Staub, A. Knoll, A. Fiolka, A. Schneider, and H. Feussner, "Design, Development and Evaluation of a Highly Versatile Robot Platform for Minimally Invasive Single-Port Surgery," in *IEEE / RAS-EMBS International Conference on Biomedical Robotics and Biomechatronics (BIOROB)*, Roma, Italy, 2012, pp. 817-822.

[5] K. Xu, J. Zhao, and Z. Dai, "A Foldable Stereo Vision Unit for Single Port Access Laparoscopy," in *IEEE International Conference on Robotics and Automation (ICRA)*, Hong Kong, China, 2014, pp. 4182-4187.

[6] X. Ma, C. Song, P. W. Chiu, and Z. Li, "Autonomous Flexible Endoscope for Minimally Invasive Surgery With Enhanced Safety," *IEEE Robotics and Automation Letters,* Vol. 4, pp. 2607-2613, 2019.

[7] X. Zhang, W. Li, P. W. Y. Chiu, and Z. Li, "A Novel Flexible Robotic Endoscope with Constrained Tendon-Driven Continuum Mechanism," *IEEE Robotics and Automation Letters,* Vol. 5, No.2, pp. 1366-1372, 2020.

[8] D. E. Whitney, "Resolved Motion Rate Control of Manipulators and Human Prostheses," *IEEE Transactions on Man-Machine Systems,* Vol. 10, No.2, pp. 47-53, June 1969.

[9] F. Flacco, A. De Luca, and O. Khatib, "Control of Redundant Robots Under Hard Joint Constraints: Saturation in the Null Space," *IEEE Transactions on Robotics,* Vol. 31, No.3, pp. 637-654, June 2015.

[10] Z. Wu, H. Yang, X. Liu, and K. Xu, "Dimension Reduced Instantaneous Inverse Kinematics for Configuration Variable Limits of Continuum Manipulators," in *IEEE International Conference on Robotics and Biomimetics (ROBIO)*, Dali, China, 2019, pp. 303-308.

[11] S. a. Zhang, Q. Li, H. Yang, J. Zhao, and K. Xu, "Configuration Transition Control of a Continuum Surgical Manipulator for Improved Kinematic Performance," *IEEE Robotics and Automation Letters,* Vol. 4, No.4, pp. 3750-3757, Oct 2019.

[12] R. J. Webster and B. A. Jones, "Design and Kinematic Modeling of Constant Curvature Continuum Robots: A Review " *International Journal of Robotics Research,* Vol. 29, No.13, pp. 1661-1683, 2010.

[13] K. Xu and N. Simaan, "Analytic Formulation for the Kinematics, Statics and Shape Restoration of Multibackbone Continuum Robots via Elliptic Integrals," *Journal of Mechanisms and Robotics,* Vol. 2, No.011006, pp. 1-13, Feb 2010.

[14] D. N. Nenchev, "Restricted Jacobian Matrices of Redundant Manipulators in Constrained Motion Tasks," *The International Journal of Robotics Research,* Vol. 11, No.6, pp. 584-597, 1992.